Composites Part A 112 (2018) 197–206

Contents lists available at ScienceDirect

Composites Part A

journal homepage: www.elsevier.com/locate/compositesa

# Conductive shear thickening gel/polyurethane sponge: A flexible human motion detection sensor with excellent safeguarding performance

Shuaishuai Zhang, Sheng Wang, Yunpeng Wang, Xiwen Fan, Li Ding, Shouhu Xuan*, Xinglong Gong*

*CAS Key Laboratory of Mechanical Behavior and Design of Materials, Department of Modern Mechanics, University of Science and Technology of China (USTC), Hefei 230027, PR China*

ARTICLE INFO

*Keywords:*
A. Multifunctional composites
B. Impact behavior
B. Rheological properties
B. Electrical properties

ABSTRACT

A novel composite with excellent sensing property and safeguarding performance is fabricated by impregnating the carbon black (CB)/shear thickening gel (STG) hybrid into polyurethane sponge (PUS). This STG-CB/PUS composite presents typical shear thickening characteristic, as the storage modulus (G′) rises from 0.21 MPa to 1.52 MPa when shear frequency increases from 0.1 Hz to 100 Hz. Under external strain, the conductivity of STG-CB/PUS varies quickly, thus it can be applied as strain sensors. During the impact, STG-CB/PUS can detect impact stimuli (0.147–1450 mJ) and decrease attacking force by 63% simultaneously. Additionally, it is found that the 'B—O cross bond' is responded for the shear thickening property and the structure-dependent electrical behaviors contribute to the sensing activity. Finally, a STG-CB/PUS enhanced kneepad is prepared. It possesses a reliable safeguarding performance by reducing 44% attacking force and can effectively trace human body motions such as walking, running and jumping.

## 1. Introduction

Body armors are widely used in police affairs and military actions to protect against external impact. Hard body armors, with ceramic [1] or steel [2] sandwiched between fabrics, were first applied to prevent high-speed bullets/projectiles from penetrating. Nevertheless, due to their rigidity and heaviness, these structures discomforted the wearers and impeded daily works. To satisfy the customized fit, a number of soft body armors [3–5], such as the Kevlar29, Vectran, and Polyester triaxial woven fabrics based soft armors [3], were developed. These soft body armors exhibited wonderful protective performance under impact and the safeguarding performance could be further enhanced by introducing resin matrix [4]. Various computational and experimental models [6–8] were also developed to discover the underlying mechanisms. Among the anti-impact materials, polyurethane sponge (PUS) was very attractive since the advantages of flexibility and porosity, thus it has been widely applied in damping [9], energy-absorption [10] and body armors. However, due to the weak strength, the safeguarding performance of the PUS is limited.

During past decades, various efforts have been conducted to improve the PUS by integrating it with functional materials so as to enlarge its applications. Shear thickening materials, whose mechanical properties such as the viscosity, storage modulus increased with the external stress/strain rate, have drawn the worldwide attention in energy absorption. Because of the excellent shear thickening effect, the shear thickening fluid (STF) was impregnated into PUS to enhance the anti-impact performance [11]. The STF/PUS composites exhibited significant energy absorption in low-velocity drop weight impact tests, revealed a broad potential in impact protection padding material. However, the application of the STF/PUS is restricted since the sedimentation problem of the liquid STF. Shear thickening gel (STG) [12] is a kind of soft polymer and its storage modulus increases 3–4 orders of magnitude with the increase of shear frequency. Very recently, our group penetrated STG into PUS to develop high performance anti-impact materials [9]. Due to the synergistic effect between STG and PUS, the STG/PUS not only overcame the creep of STG but also improved the energy absorption. Considering the superior impact resistance performance of STG/PUS, more work should be done to enlarge its application in body armor.

Force sensing is critical in body armor because the damage can be detected during resisting impact. Flexible sensors [13–15], as the essential part of wearable devices or e-skin, exhibit desirable application perspective in human motion detection [16], health-monitoring [17], soft robotics, and so forth. Besides the body protection, the PUS also has been proven to be effective in wearable devices. By combining conductive materials, such as Ag nanowires [18], Ag nanoparticles [19],

* Corresponding authors.
*E-mail addresses:* xuansh@ustc.edu.cn (S. Xuan), gongxl@ustc.edu.cn (X. Gong).

https://doi.org/10.1016/j.compositesa.2018.06.007
Received 4 May 2018; Received in revised form 31 May 2018; Accepted 4 June 2018
Available online 06 June 2018
1359-835X/ 

carbon black (CB), graphene, etc. into the interconnected three-dimension (3D) networks of the PUS, human activities can be detected by measuring and analyzing the generated electrical signals. These strain sensors exhibited high stability (1000 cycles at 50% strain), thus they became favorable in wearable devices. Typically, the CB/PUS [20] was able to detect ultra-small motion (91 Pa pressure, 0.2% strain) and large motion (16.4 kPa pressure, 60% strain). Recently, a novel graphene/PUS [21] was also prepared via the fractured microstructure design method and this piezoresistive sensor had been demonstrated to be effective in detecting super low pressure (9 Pa). In consideration of the outstanding anti-impact performance, the conductive STG/PUS with both excellent sensing property and safeguarding performance will be attractive in multifunctional body armor and wearable devices.

In this work, a novel STG-CB/PUS composite is developed by impregnating STG-CB into stretchable PUS. Besides resisting the external impact, the STG-CB/PUS can trace dynamic impact energy and detect static strain, demonstrating its promising perspective as flexible sensors. The detailed mechanism for the multifunctional STG-CB/PUS was discussed. It was found that the shear thickening characteristic, originated from the reversible 'B—O cross bond', protected human body by buffering impact force. The structure-dependent electrical property of STG-CB/PUS resulted in its sensing behavior. At last, this versatile composite could be applied to enhance the kneepad. The final device not only exhibited outstanding anti-impact performance but also could trace and distinguish body motions, such as walking, running and jumping.

## 2. Experimental section

### 2.1. Materials

Dimethyl siloxane, boric acid and benzoyl peroxide (BPO), which were used to prepare the shear thickening gel (STG), were purchased from Sinopharm Chemical Reagent Co. Ltd, Shanghai, China. All the reagents were of analytical purity and used as received without further purification. Carbon black (CB) (product type: VXC-72) was provided by Cabot Corporation, Boston, Massachusetts, USA. The polyurethane sponges (PUS) were commercially available products.

### 2.2. Experiments

Fig. 1a presented the fabrication process of STG-CB/PUS. Firstly, a thoroughly stirred mixture, consisting of 15% pyroboric acid, 81% dimethyl siloxane and 4% of ethyl alcohol, was heated at 220 °C for 8 h to obtain STG. Then, STG-CB suspension was synthesized by dispersing STG, benzoyl peroxide (weight ratio of 25:1) and CB into acetone solvent. Then, the suspension was sonicated for 20 min. After removing the solvent, STG-CB was obtained by vulcanization at 85 °C for 2 h. The weight ratio of CB to STG was maintained at 10%, 20%, and 30%, respectively. This polymer was named as STG-xCB and x represented the weight ratio. The polyurethane sponges (PUS), cut into specific shapes, were cleaned in acetone by sonicating for 30 min. Then, the STG-CB suspension was dipped into PUS slowly. Owing to the adsorption of PUS, the suspension would be adopted and limited in PUS. This procedure was not stopped until the suspension was about to leak out. The obtained composite was dried under vacuum for 30 min to remove the solvent. This 'drop and dry' process was carried out several times until the sponges were fulfilled. Finally, STG-CB/PUS was gained after vulcanization at 85 °C for 2 h.

### 2.3. Characterization

The morphologies of PUS, STG-CB and STG-CB/PUS were characterized by field emission scanning electron microscopy (FE-SEM, XL-30 ESEM). The rheological properties of STG, STG-CB and STG-CB/PUS were tested by using a commercial rheometer (Physica MCR 302, Anton Paar Co., Austria). Cylindrical samples with a thickness of 1 mm and a diameter of about 20 mm were tested between a parallel plate (diameter: 20 mm) with the shear frequency exponentially increasing from 0.1 Hz to 100 Hz and the strain was set at 0.1%. Their creep and recovery behavior were also tested by the rheometer. Before testing, the samples were cut into pieces with cylindrical shape (thickness: 4 mm, diameter: 20 mm).

The static strain sensing performance of the STG-CB/PUS under different mechanical deformations (compression and stretch) were studied by using Material Test System (MTS criterion 43, MTS System Co., America). A drop hammer test device (ZCJ1302-A, MTS System Co., America) equipped with a force sensor and data acquisition system was applied to investigate the dynamic sensing effect and safeguarding performance. In this test, the diameter and height of the cylinder STG-

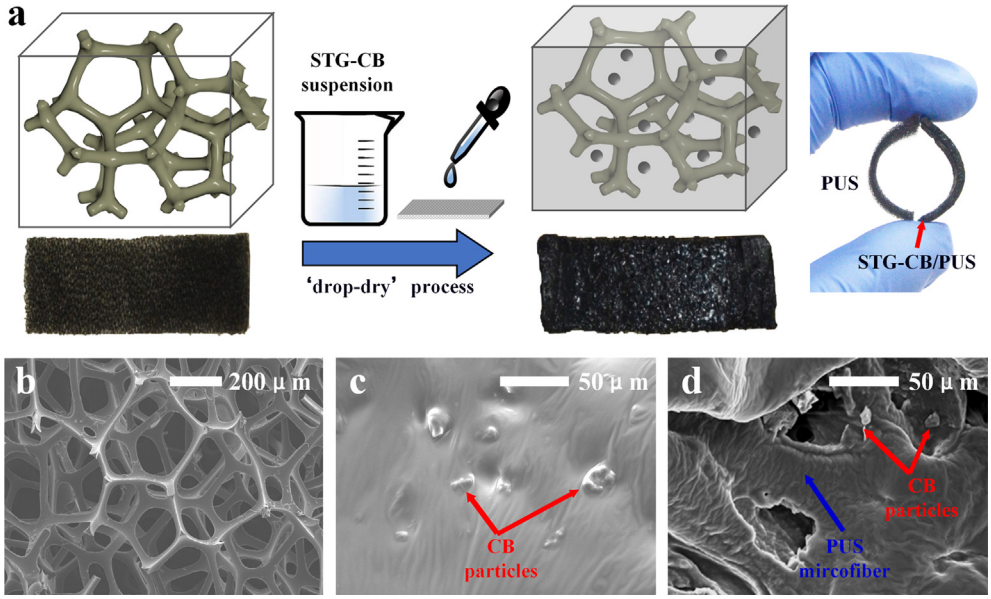


**Fig. 1.** The fabrication process of STG-CB/PUS (a). SEM morphology of PUS 3D interconnected structure (b), STG-20%CB (c) and STG-20%CB/PUS (d). (For interpretation of the references to colour in this figure legend, the reader is referred to the web version of this article.)

CB/PUS samples were kept at 21 mm and 4 mm, respectively. During the tests, the drop hammers with different mass were smashed on specimens from different heights. The force sensor could record the force signals and transform it into electrical signals. Then, the signals were recorded and analyzed in the data acquisition system.

In addition, the electrical properties were obtained by using an electrochemical impedance spectroscopy (EIS) system, with a Modulab material test system, data storage, and analyzing system (Solartron analytical, AMETEK advanced measurement technology, Inc., United Kingdom).

## 3. Results and discussion

### 3.1. Morphology

The microstructures of polyurethane sponges (PUS) was characterized in Fig. 1b. Obviously, PUS possessed a 3D interconnected and cellular-like porous network, which could provide mechanical backbone for STG. In Fig. 1c, CB particles with a diameter of 7–15 μm dispersed homogeneously in STG. And STG-CB was uniformly impregnated into PUS scaffold and some PUS microfibers were still observable in the surface (Fig. 1d). Importantly, the as-prepared STG-CB/PUS preserved the mechanical flexibility as it could be bent easily and recover after removing external stress (Fig. 1a). Therefore, the 'dip-dry' method was effective in preparing mechanically stable and flexible STG-CB/PUS.

### 3.2. Rheological and electrical property

The pristine STG possessed a typical shear thickening behavior and its storage modulus ($G'$) increased with shear frequency. As shown in Fig. 2a, when shear frequency was kept at 0.1 Hz, the initial storage modulus ($G'_{min}$) was small (677 Pa) thus the STG was plastic. As soon as the shear frequency reached to 100 Hz, the storage modulus ($G'_{max}$) increased 3 orders of magnitude ($8.07 \times 10^5$ Pa). Clearly, the STG transformed to be hard state since the remarkable shear thickening effect. Here, the carbon black (CB) was introduced into STG to improve its mechanical and electrical properties [22,23]. When the CB weight ratio was 10%, the $G'_{min}$ and $G'_{max}$ of STG-10%CB/PUS increased to 6707 Pa and $9.92 \times 10^5$ Pa, respectively. Additionally, the increase of CB weight ratio enhanced the $G'_{min}$ and $G'_{max}$ of STG-CB and this was due to the particle-strengthening effect. The porous PUS could be further used as the scaffold to enhance the mechanical property of STG-CB. For example, the $G'_{min}$ and $G'_{max}$ of STG-20%CB was $1.47 \times 10^5$ Pa and $1.63 \times 10^6$ Pa. With the introduction of PUS, the $G'_{min}$ and $G'_{max}$ of STG-20%CB/PUS increased to $2.68 \times 10^5$ Pa and $1.73 \times 10^6$ Pa, respectively. The loss modulus ($G''$) was shown in Fig. 2b. With increasing of shear frequency, the $G''$ increased to saturation and then decreased. The peak loss modulus ($G''_{max}$) of STG was $3.31 \times 10^5$ Pa. CB improved its mechanical property by increasing $G''_{max}$. For example, $G''_{max}$ of STG-10%CB was $3.97 \times 10^5$ Pa which increased by 20% compared with STG. The mechanical property of STG-20%CB was further enhanced by the introduction of PUS with its $G''_{max}$ increasing from $5.60 \times 10^5$ Pa to $5.89 \times 10^5$ Pa, which must be attributed to the energy absorption characteristic of the elastic PUS.

Creep is the tendency of the solid material to deform slowly under the loading of external stress, which has been widely researched to demonstrate the mechanical property of polymer composites. In this work, the creep (blue part) and recovery behavior (green part) of STG was investigated (Fig. 2c). Under 500 Pa shear stress, the pristine STG deformed almost linearly with time to 7.6% strain in 10 s due to the low cross-linking density. And during the recovery process, the shear strain kept almost unchanged till 100 s with an unrecoverable strain (residual strain) of 7.5%. CB enhanced its mechanical property by decreasing the shear strain to 1.0% in creep process. Differently, the shear strain of STG-20%CB recovered partly with a final residual strain of 0.53% at

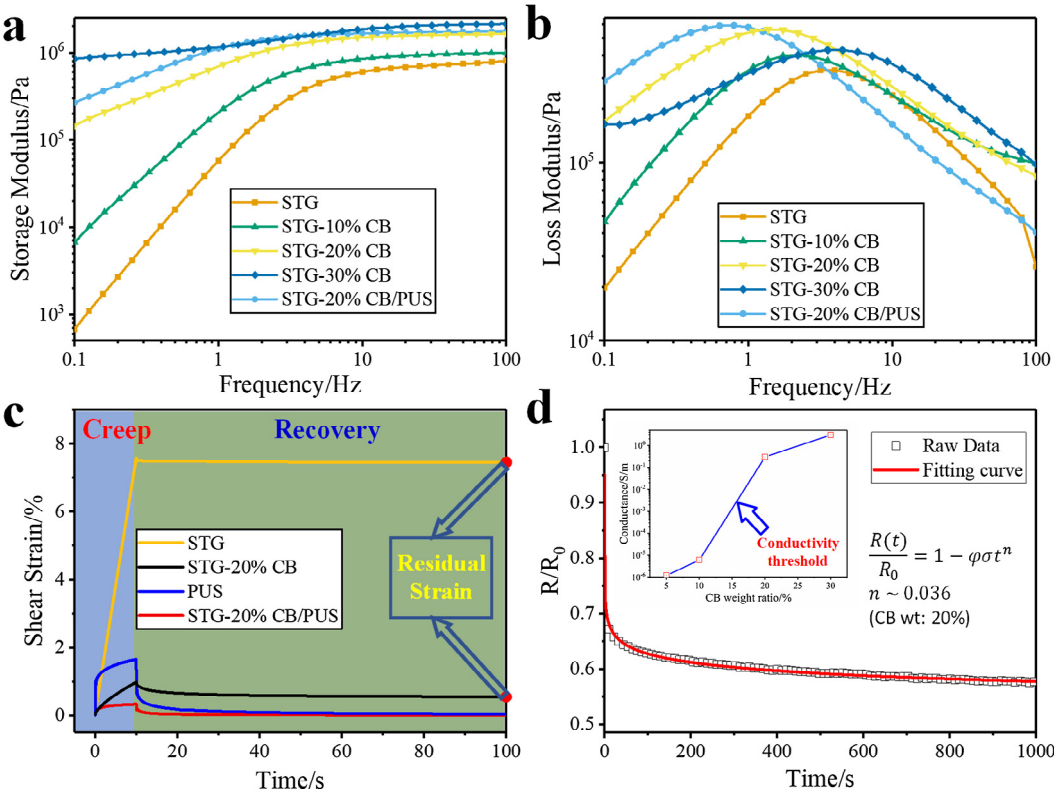


**Fig. 2.** The storage modulus (a) and loss modulus (b) of STG, STG-10%CB, STG-20%CB, STG-30%CB and STG-20%CB/PUS; creep and recovery behavior of STG, STG-20%CB, PUS, STG-20%CB/PUS under applying 500 Pa shear stress (c); $\frac{R(t)}{R_0}$ of STG-20%CB and conductivity of STG-CB with CB weight ratio of 5%, 10%, 20% and 30% (d). (For interpretation of the references to colour in this figure legend, the reader is referred to the web version of this article.)

100 s. Dramatically, PUS could fully recover to its initial state after removing shear stress. This was attributed to the high elasticity of PUS. As a result, when the porous PUS was introduced as a scaffold to support the STG-20%CB, STG-20%CB/PUS exhibited lowest creep strain (0.3%) and nearly no residual strain after recovery. Additionally, the creep behavior of STG, STG-20%CB and STG/PUS under gravity was investigated in Fig. S1. Notably, owing to the low viscosity, STG collapsed quickly from 30 mm to 18.5 mm in 20 min. Almost no creep was observed in STG-20%CB due to the particle-strengthening effect. Notably, by the introduction of mechanical backbone (PUS) to STG, the sizes of STG/PUS kept constantly with time. Therefore, the PUS improved not only the mechanical property but also the stability of STG.

Due to the presence of the carbon black, the final STG-CB became conductive. Fig. 2d showed the electrical conductivity of STG-20%CB, which was tested by using an electrochemical impedance spectroscopy system (EIS) with a sampling frequency of 100 Hz. During testing, the resistance of STG-20%CB decreased quickly at first while the decay speed reduced with time. This phenomenon perfectly meets Zhang's theory [24] which can be simplified here as

$$\frac{R(t)}{R_0} = 1-\varphi\sigma t^n \tag{1}$$

where $R(t)$ is the resistance value at time $t$, $R_0$ is the resistance value at time $t = 0$, $\varphi$ is a constant relating to the viscoelasticity of matrix, $\sigma$ here is stress induced by its gravity and $n$ is a constant dependent on conductive network structure. Obviously, the resistance decay fits the formula suitably with $n \sim 0.036$. Here, the resistance decay is mainly attributed to the time dependent interparticle separation. Because the matrix viscosity of STG is low, the conductive nanoparticles (CB) are mobile and tend to be dispersed more homogeneously in STG. Consequently, more effective conductive network is formed and thus the resistance decreases with time.

Due to the resistance decay, the conductivity of STG-CB was obtained when its resistance gradually became stable after 200 s. Obviously, As CB weight ratio increased from 10% to 20% and 30%, the conductivity increased from $6.1 \times 10^{-6}$ S/m to 0.3 S/m and 2.8 S/m, respectively. It indicated that the conductivity threshold was between 10% and 20%. Notably, the conductivity of STG-10%CB was very poor, which was unfit as flexible sensors. In addition, the $G'_{min}$ of STG-30%CB/PUS was $8.5 \times 10^5$ Pa, thus it was rigid, robust and unfit as cushioning material. Therefore, STG-20%CB/PUS was chosen as candidate for versatile body armor. For simplicity, STG-20%CB/PUS was hereinafter referred to as STG-CB/PUS.

### 3.3. Static sensing and mechanical behavior of STG-CB/PUS under compression and stretch

The electrical property of the STG-CB/PUS was sensitive to the external applied strain. Fig. 3 showed the sensing activities of the STG-CB/PUS under compression and stretch. The cylindrical STG-CB/PUS with a height of 4 mm and a diameter of 10 mm was clamped between two plates to make sure that electrodes were tightly attached to STG-CB/PUS. Due to the resistance decay effect, its resistance decreased and gradually became stable after 200 s. After that, the resistance was recorded with a final value of 88 Ω. Then, STG-CB/PUS was compressed at 1%, 2%, 3%, 4% and 5% zigzag strain respectively at a rather low speed (0.4 mm/min). The relative resistance change: $\Delta R/R_0 = (R(t)-R_0)/R_0$ rose and fell with the applied strain synchronously (Fig. 3a). And the peak $\Delta R/R_0$ increased with the strain amplitude. For example, as compression strain increased from 2% to 5%, $\Delta R/R_0$ increased from 4.19% to 9.02%. Notably, STG-CB/PUS could detect ultra-small strain as low as 0.04 mm with effective $\Delta R/R_0$ response of −1.58%. Its resistance also displayed steady and repeatable dependency on applied strain with almost no disparity in resistance response during 11 cycles.

Stretch tests were carried out on the rectangular flat STG-CB/PUS sample (45mm × 10mm × 2mm) (the right inset of Fig. 3c). As shown in Fig. 3b, the resistance increased sharply from 1793 Ω to 2043 Ω when the 1% stretch strain was applied. However, different from the compression tests, it could not recover to its initial resistance as strain was removed. The resistance of STG-CB/PUS changed regularly with the applied strain. Interestingly, both of the top and floor resistance values of 45 cycles decreased synchronously (Fig. 3b). This phenomenon was in accordance with the resistance decay of the STG-CB, which can be also explained by the Zhang's theory. Differently, much little resistance decay was found in compression tests, which may be attributed to the rather small size in strain direction (4 mm compared to 45 mm). Nevertheless, though the resistance varied in every cycle, the calculated $\Delta R/R_0$ kept almost a constant with a distribution value of 8%, thus the STG-CB/PUS possessed a stable strain-dependent sensitivity.

The relative resistance change ($\Delta R/R_0$) of STG-CB/PUS presented nearly a linear dependency on the strain amplitude (Fig. 3c). The gauge factor ($g = \Delta R/R_0/\varepsilon$) of compression and stretch tests were 1.95 and 9.26, respectively. The differences in the sample size especially the length in the strain direction may contribute to the disparity of gauge factor for the two tests. Importantly, the standard errors of the fitting results were 0.02 (compression) and 0.06 (stretch), respectively, confirming the reliability of STG-CB/PUS. As the probability distribution curves (Fig. 3d) depicted, the $\Delta R/R_0$ values scattered closer in compression tests, suggesting more stable sensing performance. Meanwhile, STG-CB/PUS could detect super low stretch strain as low as 0.5%. In summary, STG-CB/PUS showed excellent sensitivity, with well-marked linearity, stability and accuracy in both static compression and stretch tests.

The mechanical property of the STG-CB/PUS under cycle stretch and compression was investigated in Fig. 4. Fig. 4a showed the stress under cycle 3% strain stretch test. With the increase of strain, the stress rose sharply at first and then increase linearly with strain. As the strain was removed, stress dropped quickly and then fell slowly. However, the strain-stress curves differed apparently during loading and unloading processes, forming hysteresis loops [25] which gradually became stable after 6th cycle. The hysteresis loop was mainly attributed to the disentanglement and slippage between molecular chains and its area represented the energy dissipated in STG-CB/PUS during stretch cycles. Notably, after the first cycle, the stress did not recover to zero and this was attributed to the strain delay induced by the viscoelasticity of STG. A similar phenomenon was also observed in compression tests (Fig. 4d). Fig. 4b and S2 presented the detailed stress-cycle relations under different strains. Apparently, the peak stress during loading processes gradually reduced and then approached to a steady value after 6th cycle (Fig. 4c). Moreover, the peak stress increased with the applied strain. For example, the peak stress in 10th cycle increased from 8 kPa to 37 kPa when the stretch strain amplitude varied from 0.5% to 3%. As shown in Fig. 4d, with the increasing applied strain, the area of hysteresis loop increased simultaneously. As larger strain resulted in more slippage and disentanglement of molecular chains, and consequently, more energy was dissipated.

### 3.4. Dynamic sensing and anti-impact performance of STG-CB/PUS

STG-CB/PUS was also sensitive to the dynamic impact stimuli and two dynamic impact tests were conducted to investigate the dynamic sensing performance. The as-prepared columniform STG-CB/PUS, with two copper sheets (thickness: 0.1 mm) attached at both ends, was stuck between a force sensor and a thin flat plate (made of Acrylonitrile Butadiene Styrene by 3D printing) (Fig. S3). The force sensor equipped with signal acquisition and storage system was used to record the force signals. The plate, a little larger than the specimen, was used to make sure that the stress was evenly distributed on the surface.

Firstly, the agate ball with the mass of 0.30 g was dropped right above the STG-CB/PUS with the relative height of 5, 10, 15, 20, 25 cm (Fig. 5a). Fig. 5b was $\Delta R/R_0$ of the balls with the mass of 0.30 g, 0.62 g,

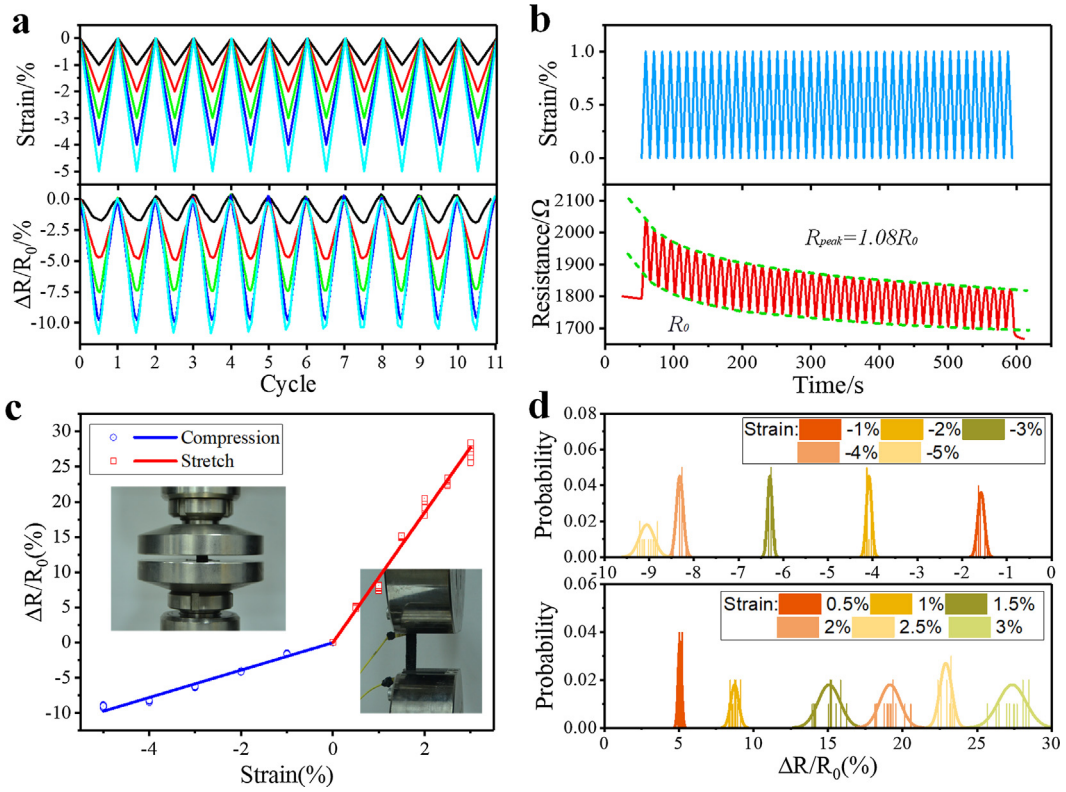


**Fig. 3.** Static sensing of STG-CB/PUS under compression and stretch. The relative resistance change response to zigzag compression strain cycles (a) and the resistance response to stretch strain cycles (b); the linear fitting plots of former results (c); the probability distribution curves of compression (upper part) and stretch (bottom part) tests (d). (For interpretation of the references to colour in this figure legend, the reader is referred to the web version of this article.)

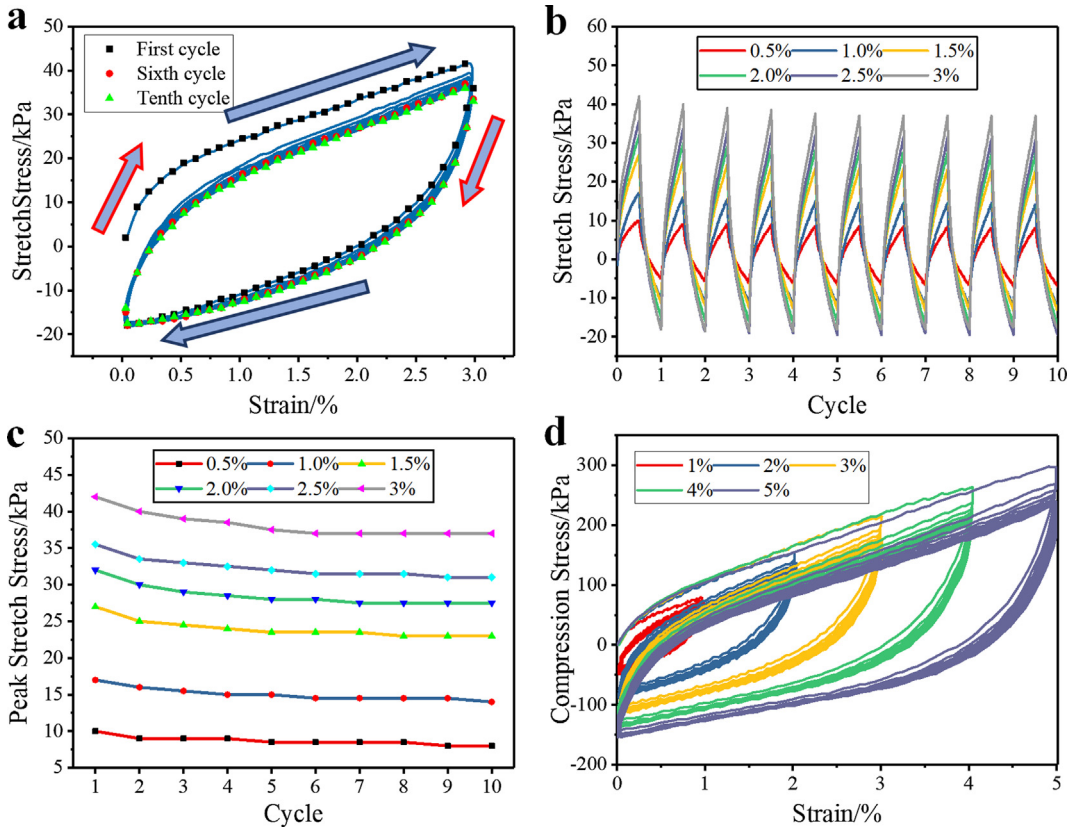


**Fig. 4.** The mechanical property of STG-CB/PUS under compression and stretch. Stretch stress under 3% cycle stretch strain loading (a); stretch stress (b) and the peak stretch stress (c) under cycle stretch strain loadings; the compression stress under cycle compression strain loading (d) of STG-CB/PUS. (For interpretation of the references to colour in this figure legend, the reader is referred to the web version of this article.)

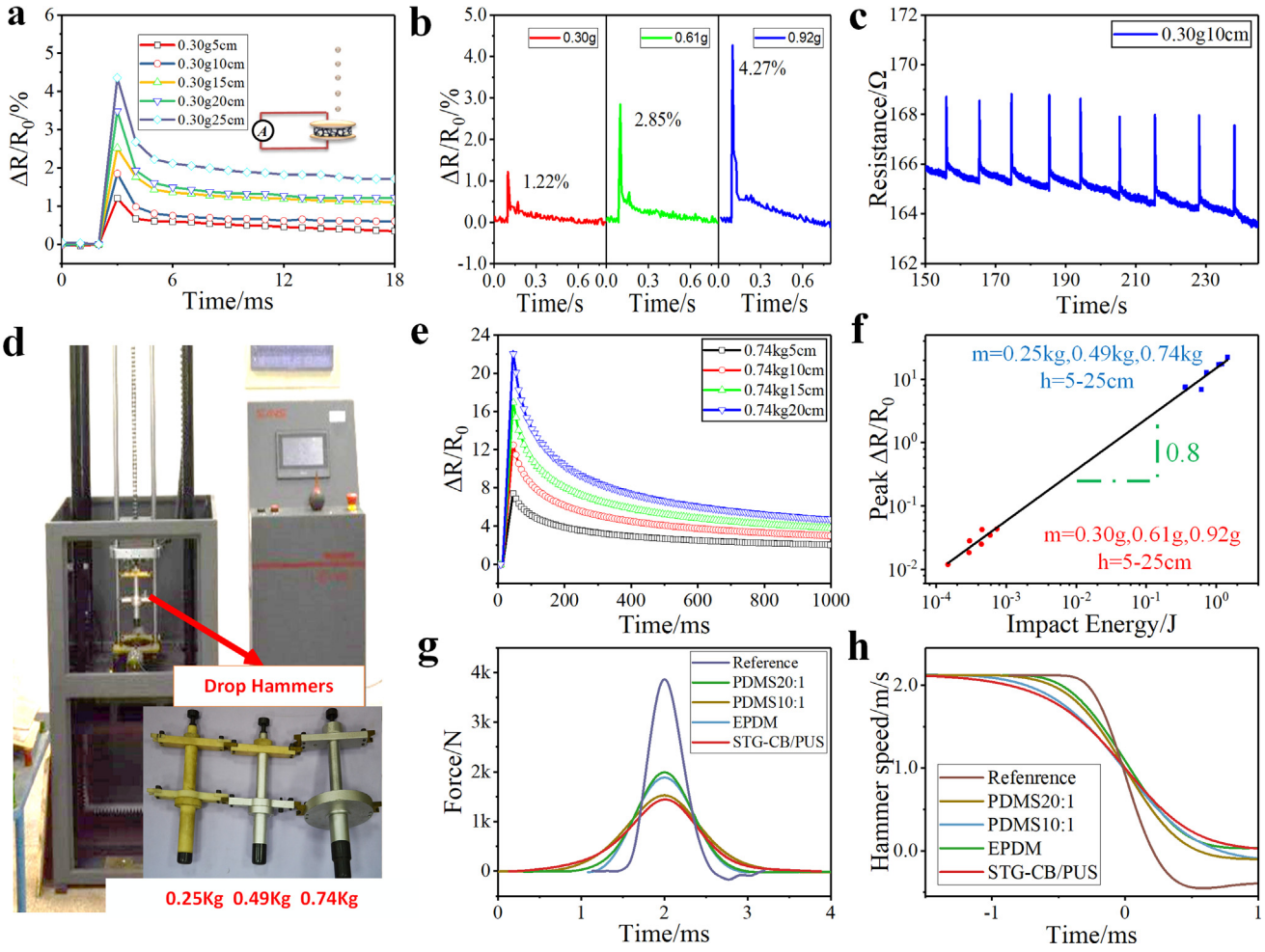


**Fig. 5.** The relative resistance change and force responses to dynamic impact. The $\Delta R/R_0$ of 0.30 g ball dropping from 5 cm, 10 cm, 15 cm, 20 cm, 25 cm (a) and balls with the mass of 0.30 g, 0.61 g, 0.92 g dropping from 5 cm (b) and 0.74 kg drop hammer dropping from 5 cm, 10 cm, 15 cm, 20 cm (e). The resistance of 0.30 g ball cyclic dropping from 10 cm (c). The picture of drop hammer machine and drop hammers (d). The fitting curve of peak $\Delta R/R_0$ versing impact energy (f). The results of force (g) and speed (h) of the 0.74 kg drop hammer dropping from 25 cm and smashing on PDMS (20:1), PDMS (10:1), EPDM and STG-CB/PUS. (For interpretation of the references to colour in this figure legend, the reader is referred to the web version of this article.)

0.93 g dropping from 5 cm. Evidently, $\Delta R/R_0$ increased abruptly when the ball smashed onto the sample and then decreased close to its initial values gradually within 0.6 s. As the drop height or drop mass increased, the peak $\Delta R/R_0$ values rose simultaneously. For example, $\Delta R/R_0$ increased from 1.22% to 3.48% as the drop height of 0.30 g drop ball varied from 5 cm to 20 cm. To further study the reliability of STG-CB/PUS, its cycle performance was measured by using the drop ball with the mass of 0.30 g falling from 10 cm at about 5 s intervals (Fig. 5c). During the test, the resistance exhibited fluctuating changes while the relative magnitude almost kept constantly. The mean value of $\Delta R/R_0$ were 2.15% with a standard error of 0.13, indicating the reliable and steady sensing performance of STG-CB/PUS.

Then, another drop test was performed on STG-CB/PUS by using the drop hammer machine (Fig. 5d) with the weight of drop hammers varied from 0.25 kg to 0.49 kg and 0.74 kg, respectively. Fig. 5e presented $\Delta R/R_0$ of 0.74 kg drop hammer falling from different heights. The influence of drop mass was also researched (Fig. S4). Similarly, the increase of drop height or drop mass led to the raise of $\Delta R/R_0$, which was in accordance with the results in Fig. 5a and b. For example, as the drop height of 0.74 kg drop hammer varied from 5 cm to 20 cm, $\Delta R/R_0$ increased from 7.42 to 22.0. As shown in Fig. S5, the drop hammer with the mass of 0.74 kg fell from 25 cm at about 50 s intervals to evaluate its stability. The mean value and standard error of peak relative resistance change were 20.86 and 0.75, respectively. The results indicated there was no unacceptable discrepancies in the magnitude and waveform of the responses during repeated impact loading cycles. In conclusion, STG-CB/PUS composite exhibited remarkable sensitivity and stability in both lightweight and heavyweight impact tests. This property allowed STG-CB/PUS to be further applied as impact sensor.

According to the theory of Boland [26]:

$$\Delta R/R_0 \propto (E_{mgh})^k \tag{2}$$

where $E_{mgh} = mgh$ is the impact energy and $m$ is the drop mass, $g$ is the gravity constant, $h$ is the drop height. And $k$ is a constant related to the structure of the conductive network. Plotted in Fig. 5f is the fitted line. The red and blue points are the results of lightweight and heavyweight impact tests, respectively. As expected, the data follows a power law with $k \sim 0.8$. The fitting result is quite reasonable with a standard error of 0.04, indicating that the resistance behavior in dynamic impact conditions relates to impact energy directly as the theory depicts. And the impact energy $E_{mgh} = mgh$ is proportional to drop mass and drop height. So, the increase of drop mass or drop height results in larger $\Delta R/R_0$, consistent with the experiment results.

PUS was widely used as cushioning material and STG exhibited excellent force dissipation characteristic due to the shear thickening property. So, a force sensor was applied below the STG-CB/PUS to quantitatively illustrate the protective performance of STG-CB/PUS. Plotted in Fig. 5g was the force response to drop hammer impacts

(0.74 kg, 25 cm). As a comparison, polydimethylsiloxane (PDMS, curing agent ratio: 20:1), PDMS (curing agent ratio: 10:1) and ethylene propylene diene monomer (EPDM) rubber specimens with the same size performing as protective layers were also tested. Additionally, a control group without a protective layer was applied as a reference. As drop hammer stroked on the force sensor directly without a protective layer, the force increased sharply to peak value (3859 N) in 1 ms and then decreased quickly before hammer bounced back. Compared with the other specimens, STG-CB/PUS displayed smallest peak force of 1444 N, which was reduced by 63% compared with the control group (3859 N), indicating its excellent force dissipation property. When the hammer strikes on STG-CB/PUS, shear thickening effect occurs and the dramatic increase of the rate-dependent rigidity can endure and damp out the impact force effectively. Traditionally, PDMS is usually applied as matrix of flexible sensors and EPDM is used as cushioning material, while the experiment results indicate STG could also be applied in flexible sensors while buffering external impacts simultaneously.

The speed-time curves were plotted according to force data (Fig. 5h). Obviously, the initial speed of drop hammer impacting on different samples were the same (2.1 m/s). Differently, as the drop hammer smashed directly on the force sensor, the final speed was −0.4 m/s as the hammer bounced back. And the impact duration time was 1.0 ms. Compared with other specimens, STG-CB/PUS showed the longest impact duration time (2.5 ms) due to its rate-dependent rigidity, which finally resulted in lowest peak force. According to momentum conservation law:

$$m\Delta v = \int F dt \tag{3}$$

where $\Delta v$ is the speed change, $m\Delta v$ is the same when drop height and drop mass are the same. $F$ is the force and $t$ is the time. So longer impact time means lower impact force, which agrees with the experiment results. To further illustrate the performance of different specimens under impact, the drop height was varied from 5 cm to 25 cm with the peak force values recorded (Fig. S6). Dramatically, peak force values of STG-CB/PUS in different tests were smaller than other specimens, suggesting its distinguishable impact resistance. In conclusion, STG-CB/PUS exhibited stable, effective and reproducible resistance dependency on external impact stimuli and excellent safeguarding performance. Therefore, it could be further developed as a promising candidate for smart versatile body armor.

### 3.5. Mechanical and electrical mechanisms of STG-CB/PUS

Fig. 6a and b present the schematic of shear thickening property of STG. When the boric acid is introduced into dimethyl siloxane, B atoms form structures [9] shown in Fig. 6a. Owing to the electron-deficient p orbital of the B atoms and redundant electrons in the orbital of O atoms, 'B—O cross bonds' (Fig. 6a) are formed among molecular chains. These noncovalent, transient bonds, similar to the hydrogen bonds in water, arrange molecular chains into uniform structural network. At low strain rate, molecular chains in STG have enough time to relax and disassemble the entanglements (Fig. 6b). Simultaneously, the breakage and reformation of transient 'B—O cross bonds' allow the network a certain internal mobility. So, the stress-induced slight frictional interactions and mechanical interferences among different molecular chains contribute to the rather low storage modulus of STG. In this case, STG is soft, plastic and tend to deform easily under stress. However, at high strain rate, disordered polymer molecular chains slip more severely and cannot adjust themselves to dynamic loadings. Consequently, large numbers of 'B—O cross bonds' are broken to endure the external stimuli and dissipate impact energy which results in the significantly increased storage modulus of STG.

STG-CB/PUS also exhibits strain and rate dependent electrical properties. In the static condition, the conductivity of STG-CB/PUS is improved under compression and weakened under stretch. This is mainly attributed to the change of particle separation as shown in schematic representation (Fig. 6c). Clearly, its resistance $R$ could be expressed as

$$R = \sum (R_p + R_b) \tag{4}$$

where $R_b$ is the bulk resistance of STG between CB particles which is originated from quantum tunneling effect and $R_p$ is the particle resistance. As STG-CB/PUS is subjected to an external strain, the inter-particle separation of the tunneling bridge is reduced (compression) or enlarged (stretch), which finally results in the increase or decrease of $R_b$ and $R$.

Interestingly, a different effect leads to electrical properties in dynamic conditions (Fig. 6d). Under impact, the impact energy of drop balls or hammers is dissipated by STG-CB/PUS and results in the breakage of conductive network structure. Consequently, the decrease of conductive paths leads to the increasing resistance. Then, the small range motion of CB particles in viscoelastic STG and the recovery behavior of STG-CB/PUS lead to the reformation of inter-particle connections. Finally, the resistance falls with time.

### 3.6. Applications of STG-CB/PUS

STG-CB/PUS was sensitive to external stimuli, exhibiting prospective as tactile sensors. STG-CB/PUS, cut into cylindrical shape with a diameter of 21 mm and height of 4 mm, was touched by human finger with its resistance response recorded (Fig. 7a). Clearly, the resistance increased from 3.9 kΩ to 4.4 kΩ under pressing (red lines) and then dropped gradually to its initial value after removing the pressure (blue lines). Another sample, cut into rectangular shape with the size of 30 mm × 10 mm × 2 mm, was attached to index finger with adhesive tape. The resistance response to finger bending (Fig. 7b) consisted of four processes: bend, stay, extend and stay. As shown in the image, the resistance increased quickly from 15 kΩ to 19 kΩ when the finger was bending. Then, it decayed to 11 kΩ as the electrical network relaxed at the stay process. Interestingly, when index finger extended to its initial state, the resistance increased again in a way similar to the response to bending before falling off. Notably, under repeated finger press or bending, STG-CB/PUS remain sensitive and reliable, since reproducible resistance response was observed. Therefore, STG-CB/PUS is a promising candidate as a tactile sensor by recording the generated electrical signals.

Owing to the sensitivity and anti-impact property, STG-CB/PUS possessed a high potential in wearable safeguarding device. Therefore, a commercial kneepad enhanced with STG-CB/PUS was fabricated and investigated. As shown in Fig. S7, the pristine kneepad was made of a layer of thermoplastic polyurethanes (TPU) outer covering and a layer of ethylene vinyl acetate (EVA) high-density sponge inner cushion. It was enhanced by replacing the middle part of the inner cushion with STG-CB/PUS. To compare the performance, both the pristine kneepad and enhanced kneepad were tested respectively, by attaching them to a human knee equipped with an impact hammer and a force sensor (Fig. 7c and Movie 1). The impact hammer attached with a piezotronic force sensor could provide and record the impact force. At the same time, the charge sensor under the kneepad recorded the penetrated force which was loaded on a human knee. The protective performance could be analyzed quantitatively and accurately by comparing the two force signals. As shown in Fig. 7d and e, the specimens were tested under three different impact force levels: low (150 N), medium (250 N) and high (330 N). Two peaks were observed in impact force. The first peak was the true force acting on kneepad. While the second represented the limitation of hammer movements by man hand after bouncing back. Obviously, the increase of external stimuli lifted the magnitude of the penetrated force loaded on the knee while reduced its duration. The former phenomenon was reasonable and the latter was induced by the increase of impact speed. Obviously, the knee endured

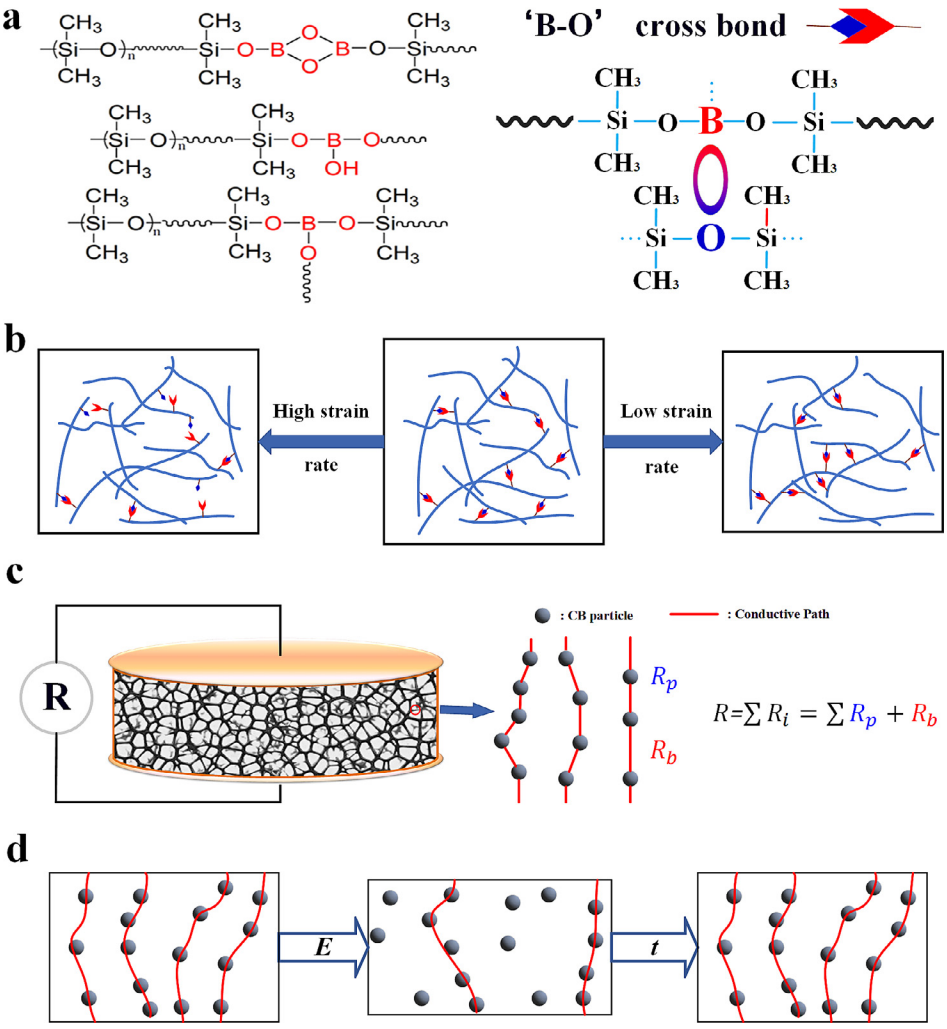


**Fig. 6.** The chemical formula and 'B—O cross bonds' structure in STG (a). The mechanism of shear thickening behavior (b). The electrical behavior of STG-CB/PUS in static (c) and dynamic (d) condition. Sketch of STG-CB/PUS sandwiched between two copper electrodes (c). The electrical model comprised of a series of connections between the bulk resistance (induced by tunneling effect, $R_b$) and the particle resistance ($R_p$). Schematic illustrating the energy induced connection breakage and time-dependent reformation of inter-particle connections (d). (For interpretation of the references to colour in this figure legend, the reader is referred to the web version of this article.)

smaller force and shorter impact duration time when the enhanced kneepad was used. For example, when the enhanced kneepad was impacted with the peak force of 330 N, the maximum penetrated force was 79.7 N, which was reduced by 44% compared with the pristine kneepad (142.7 N). In addition, the time that penetrated force increased to its peak value reduced from 2.6 ms to 1.5 ms, which also demonstrated the superior safeguarding performance of STG-CB/PUS. Besides, due to its resistance sensitivity to outer force pulse excitation, the resistance was monitored during tests (green lines in Fig. 7e). Obviously, the resistance of STG-CB/PUS rose steeply within 3 ms under impact and then descended gradually with time. Due to the data acquisition frequency limitation, the resistance was recorded every millisecond, but the fast response time of ~3 ms upon loading was still remarkable. In addition, upon growing impact loadings, $\Delta R/R_0$ exhibited rising peak values, which were 0.09, 0.29 and 0.57, respectively, showing well impact force sensitivity.

Due to the sensitivity of STG-CB/PUS, the enhanced kneepad could be further used in body motion detection, such as walking, running, and jumping (Fig. 7f–h). In walking, the resistance increased from 283 Ω to 290 Ω and then dropped to 282 Ω as the foot was lifted. Dramatically, as foot fell, the resistance rose again to 284 Ω and decrease to a lower value (281 Ω). Importantly, the resistance response in running was in a regular pattern with a cycle of about 1 s, while that in walking was almost 2 s. This phenomenon was in reasonable agreement with the real situation as running was faster than walking. Interestingly, in jumping, the resistance increased from 272 Ω to 320 Ω and then fell to initial value without a second peak. Additionally, it demonstrated reproducible responses to repeated body motions, indicating its stable and reliable sensing property. In conclusion, the enhanced kneepad could not only provide effective protection by buffering impact force but also monitor external stimuli simultaneously. Moreover, it also could be used in body motion detection with effective, reproducible and distinguishable resistance responses.

## 4. Conclusions

In this work, based on STG-CB/PUS, a new flexible body motion detection sensor with excellent safeguarding performance was developed. STG-CB/PUS with reasonable conductivity and superior shear thickening property exhibited steady and effective responses to both static and dynamic stimuli. Importantly, it could detect low strain as low as 0.5% and buffer impact force by nearly 63%. The 'B—O cross bonds' are found to be the main reason for shear thickening property of STG and the structure-dependent electrical behaviors of STG-CB/PUS

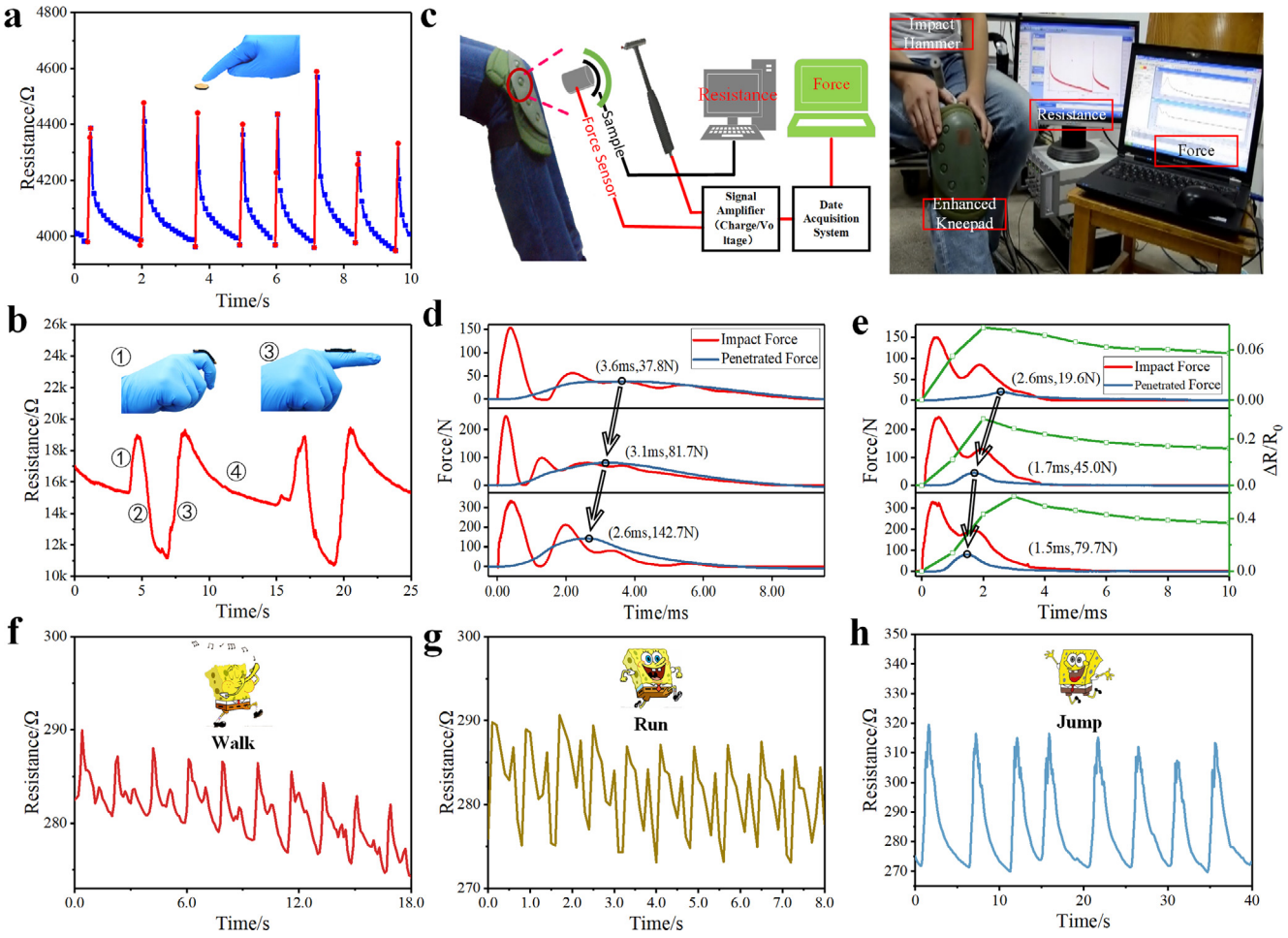


**Fig. 7.** The resistance response to finger press (a) and bending (b); test system of sensing and anti-impact performance of kneepad (c); anti-impact performance of pristine kneepad (d); anti-impact and dynamic sensing performance of enhanced kneepad (e) and its electrical response to body motions: walking (f), running (g) and jumping (h). (For interpretation of the references to colour in this figure legend, the reader is referred to the web version of this article.)

contributes to the sensing activity. Moreover, a kneepad enhanced with STG-CB/PUS effectively traced human motion such as jumping, walking and running. And it could decline the impact force by almost 44% compared with the pristine kneepad and detect various external stimuli within 3 ms. This multifunctional sensor with excellent electro-mechanical property and safeguarding performance shows promising applications in a range of devices such as versatile body armors.

## Acknowledgements

Financial supports from the National Natural Science Foundation of China (Grant No. 11772320), the Strategic Priority Research Program of the Chinese Academy of Sciences (Grant No. XDB22040502), and the Fundamental Research Funds for the Central Universities (WK2480000002, WK2090050045) are gratefully acknowledged. This study was also supported by the Collaborative Innovation Center of Suzhou Nano Science and Technology.

## Appendix A. Supplementary material

Supplementary data associated with this article can be found, in the online version, at https://doi.org/10.1016/j.compositesa.2018.06.007.

## References

[1] Zheng L, Huan H, Zeng Y, Song S, Cheng S, Zhang C. A study on the failure mechanism and wear loss of impregnated diamond bits during machining process of armor ceramics. J Mech Sci Technol 2018;32(1):261–8.
[2] Wang H, Hazell PJ, Shankar K, Morozov EV, Escobedo JP, Wang C. Effects of fabric folding and thickness on the impact behaviour of multi-ply UHMWPE woven fabrics. J Mater Sci 2017;52(24):13977–91.
[3] El Messiry M, Eltahan E. Stab resistance of triaxial woven fabrics for soft body armor. J Ind Text 2014;45(5):1062–82.
[4] Gopinath G, Zheng JQ, Batra RC. Effect of matrix on ballistic performance of soft body armor. Compos Struct 2012;94(9):2690–6.
[5] Yang Y, Chen X. Investigation of energy absorption mechanisms in a soft armor panel under ballistic impact. Text Res J 2016;87(20):2475–86.
[6] Cunniff PM. A semiempirical model for the ballistic impact performance of textile-based personnel armor. Text Res J 2016;66(1):45–58.
[7] Tapie E, Tan ESL, Guo YB, Shim VPW. Effects of pre-tension and impact angle on penetration resistance of woven fabric. Int J Impact Eng 2017;106:171–90.
[8] Sockalingam S, Gillespie Jr JW, Keefe M. Modeling the fiber length-scale response of Kevlar KM2 yarn during transverse impact. Text Res J 2017;87(18):2242–54.
[9] Wang S, Xuan S, Wang Y, Xu C, Mao Y, Liu M, et al. Stretchable polyurethane sponge scaffold strengthened shear stiffening polymer and its enhanced safe-guarding performance. ACS Appl Mater Inter 2016;8(7):4946–54.
[10] Du X, Liu HY, Mai YW. Ultrafast synthesis of multifunctional N-doped graphene foam in an ethanol flame. ACS Nano 2016;10(1):453–62.
[11] Fahool M, Sabet AR. Parametric study of energy absorption mechanism in Twaron fabric impregnated with a shear thickening fluid. Int J Impact Eng 2016;90:61–71.
[12] Wang S, Jiang W, Jiang W, Ye F, Mao Y, Xuan S, et al. Multifunctional polymer composite with excellent shear stiffening performance and magnetorheological effect. J Mater Chem C 2014;2(34):7133–40.
[13] Trung TQ, Lee NE. Flexible and stretchable physical sensor integrated platforms for wearable human-activity monitoringand personal healthcare. Adv Mater 2016;28(22):4338–72.
[14] Fernandez RE, Umasankar Y, Manickam P, Nickel JC, Iwasaki LR, Kawamoto BK, et al. Disposable aptamer-sensor aided by magnetic nanoparticle enrichment for detection of salivary cortisol variations in obstructive sleep apnea patients. Sci Rep 2017;7(1):17992.
[15] Kuang J, Dai Z, Liu L, Yang Z, Jin M, Zhang Z. Synergistic effects from graphene and carbon nanotubes endow ordered hierarchical structure foams with a combination

of compressibility, super-elasticity and stability and potential application as pressure sensors. Nanoscale 2015;7(20):9252–60.
[16] Vilarinho D, Theodosiou A, Leitão C, Leal-Junior AG, Domingues MdF, Kalli K, et al. POFBG-embedded cork insole for plantar pressure monitoring. Sensors 2017;17(12):2924.
[17] Wu J, Wang J, Ling Y, Xu H. An advanced hybrid technique of dcs and jsrc for telemonitoring of multi-sensor gait pattern. Sensors 2017;17(12):2764.
[18] Ge J, Yao HB, Wang X, Ye YD, Wang JL, Wu ZY, et al. Stretchable conductors based on silver nanowires: improved performance through a binary network design. Angew Chem Int Ed 2013;52(6):1654–9.
[19] Li L, Zhu C, Wu Y, Wang J, Zhang T, Liu Y. A conductive ternary network of a highly stretchable AgNWs/AgNPs conductor based on a polydopamine-modified polyurethane sponge. RSC Adv 2015;5(77):62905–12.
[20] Wu X, Han Y, Zhang X, Zhou Z, Lu C. Large-area compliant, low-cost, and versatile pressure-sensing platform based on microcrack-designed carbon black@polyurethane sponge for human-machine interfacing. Adv Funct Mater 2016;26(34):6246–56.
[21] Yao HB, Ge J, Wang CF, Wang X, Hu W, Zheng ZJ, et al. A flexible and highly pressure-sensitive graphene-polyurethane sponge based on fractured microstructure design. Adv Mater 2013;25(46):6692–8.
[22] Bokobza L, Rahmani M, Belin C, Bruneel J-L, El Bounia N-E. Blends of carbon blacks and multiwall carbon nanotubes as reinforcing fillers for hydrocarbon rubbers. J Polym Sci Part B: Polym Phys 2008;46(18):1939–51.
[23] Sengupta R, Bhattacharya M, Bandyopadhyay S, Bhowmick AK. A review on the mechanical and electrical properties of graphite and modified graphite reinforced polymer composites. Prog Polym Sci 2011;36(5):638–70.
[24] Zhang XW, Pan Y, Zheng Q, Yi XS. Time dependence of piezoresistance for the conductor-filled polymer composites. J Polym Sci Part B: Polym Phys 2000;38(21):2739–49.
[25] Xu Y, Tao R, Lubineau G. Nonlinear viscoelasticity of pre-compressed layered polymeric composite under oscillatory compression. Compos Sci Technol 2018.
[26] Boland CS, Khan U, Ryan G, Barwich S, Charifou R, Harvey A, et al. Sensitive electromechanical sensors using viscoelastic graphene-polymer nanocomposites. Science 2016;354(6317):1257–60.